nature communications

Article

https://doi.org/10.1038/s41467-024-54663-7

Accurate stacking engineering of MOF nanosheets as membranes for precise H_2 sieving

Received: 22 May 2024

Accepted: 15 November 2024

Published online: 30 December 2024

Check for updates

Wufeng Wu[1,4], Xitai Cai[1,4], Xianfeng Yang[2], Yanying Wei[1] ✉, Li Ding[3], Libo Li[1] ✉ & Haihui Wang[3] ✉

Two-dimensional (2D) metal-organic framework (MOF) nanosheet membranes hold promise for exact molecular transfer due to their structural diversity and well-defined in-plane nanochannels. However, achieving precise regulation of stacking modes between neighboring nanosheets in membrane applications and understanding its influence on separation performance remains unrevealed and challenging. Here, we propose a strategy for accurately controlling the stacking modes of MOF nanosheets via linker polarity regulation. Both theoretical calculations and experimental results demonstrate that a high linker polarity promotes neighboring nanosheets to a maximum AB stacking due to steric hindrance effects, leading to a controlled effective pore size of the membrane and consequently to improved molecular sieving. Among series of CuBDC-based 2D MOFs with different linkers, the CuBDC-NO_2 nanosheet membranes exhibit a reduced effective stacking aperture of 0.372 nm, yielding H_2 permeance of 4.44×10^{-7} mol m^{-2} s^{-1} Pa^{-1} with a high H_2/CO_2 and H_2/CH_4 selectivity of 266 and 536, respectively. This work represents the in-depth investigation of the accurate tuning of MOF nanosheet stacking in the field of 2D materials, offering more perspectives for broader applications with universality for various 2D materials.

Membrane processes have gained increasing attraction in gas separation owing to their operational simplicity and low energy consumption[1–5]. Among the common materials employed for membrane construction, polymeric membranes garnered interest for their potential for large-scale production ability, but they are often limited by the Robeson bound[6–9]. In recent years, porous nanosheets with nanoscale thickness have been utilized as building blocks to prepare membranes aiming to surpass the separation performance upper bound of traditional membranes[10–13]. Within numerous two-dimensional (2D) materials, metal-organic framework (MOF) nanosheets, with highly ordered 2D network structure of coordinated organic linkers and metal ions/clusters, tunable chemical properties and abundant regular in-plane nanochannels, are expected to allow fast mass transfer and highly selective molecular sieving[10,14,15]. Yang et al. pioneered in achieving rapid gas molecule transport through MOF nanosheet membranes, demonstrating excellent H_2/CO_2 selectivity[10]. Subsequently, Zhao et al. fabricated the MAMS-1 nanosheet membrane, which also displayed promising gas separation capabilities[15].

Although a few membranes are reported based on MOF nanosheets, the study on MOF nanosheet membranes remains in its early stage, where several crucial issues remain unexplored or unrecognized. During the assembly of MOF nanosheets, the stacking modes of

[1]State Key Laboratory of Pulp and Paper Engineering, School of Chemistry and Chemical Engineering, Guangdong Provincial Key Lab of Green Chemical Product Technology, South China University of Technology, Guangzhou 510640, China. [2]Analytical and Testing Centre, South China University of Technology, Guangzhou 510640, China. [3]Beijing Key Laboratory for Membrane Materials and Engineering, Department of Chemical Engineering, Tsinghua University, Beijing 100084, China. [4]These authors contributed equally: Wufeng Wu, Xitai Cai. ✉e-mail: ceyywei@scut.edu.cn; celbli@scut.edu.cn; cehhwang@tsinghua.edu.cn

neighboring nanosheets have not received adequate attention and in-depth investigation yet. They can be highly overlapped or staggered, even with different staggering degrees, and with stacking pore structures. Such different stacking modes obviously affect the mass transport channels with alterations in the effective sieving apertures, and consequent membrane separation performance. Unfortunately, there is few experimental or computational work discussing this issue in the field of MOF nanosheet membranes. To the best of our knowledge, only Wang's group tried to regulate the AA (highly overlapped) and AB (maximum staggered) binary stacking modes of $[Cu_2Br(IN)_2]_n$ nanosheets through drop casting by controlling the solvent droplet dynamic behavior, thus demonstrating the significant influence of the nanosheets stacking mode on the gas separation performance[16]. However, achieving continuous regulation of stacking structures in MOF nanosheet membranes, especially the precise control of the stacking modes with different degrees, still remains challenging, either experimentally or through theoretical calculations. Herein, the staggered stacking modes of MOF nanosheets are regulated by adjusting the polarity of linkers, thereby controlling the effective sieving size of the membrane and achieving efficient H_2 sieving, where the typical CuBDC-based (BDC is benzene dicarboxylic acid) MOF nanosheets are chosen as basic material. The free in-plane pore diameter of CuBDC is 0.8 nm, which becomes smaller - but with a wide pore size distribution - through a random stacking of CuBDC nanosheets. Therefore, controlled stacking is required.

Results

Theoretical prediction driven MOF nanosheet stacking engineering

A series of linkers including BDC-$(OH)_2$, BDC-$(Br)_2$, BDC-NH_2, BDC-NO_2, BDC-OH and BDC-Br with different side chains are screened through simulations to form CuBDC-based stacks. Based on the mother structure of CuBDC, the crystal structures of bulk CuBDC-$(OH)_2$, CuBDC-$(Br)_2$, CuBDC-NH_2, CuBDC-NO_2, CuBDC-OH and CuBDC-Br are constructed using density functional theory (DFT) calculations (Supplementary Fig. 1 and Supplementary Table 1). These structures are similar to the previously reported CuBDC structure[17], consisting of Cu coordinated with BDC-based linkers to form a porous 2D network that stacks along the normal direction of $(\bar{2}01)$ plane, maintained by van der Waals force, yielding a regular lattice structure. Through computational analysis, the theoretical apertures of a series of monolayer nanosheets are 0.700, 0.580, 0.695, 0.545, 0.737 and 0.651 nm (Supplementary Fig. 1) identified on the $(\bar{2}01)$ plane, which illustrates that the introduction of distinct functional groups can regulate the in-plane nanosheet apertures to different extents.

To understand the influence of the diverse side chains on the stacking mode, the stability of such stacked nanosheets with different stacking modes is investigated. Six representative possible stacking modes are chosen from numerous probable stacking configurations (Fig. 1a), which can be designated as AA and AB_x ($x \in (0, 1)$) categorized according to their sliding degree from 0 to 100% between neighboring MOF nanosheets (Fig. 1b). To be specific, AA stacking corresponds to sliding degree of x = 0, signifying no sliding, while AB stacking with sliding degree of x = 100%, represents maximum sliding degree. When the sliding degree of $x \in (0, 100\%)$, a series of infinite stacking modes between AA and AB appear. Taking CuBDC-NO_2 for an illustrative instance (Fig. 1c, d), the climbing-image nudged elastic band (CI-NEB) method is utilized to analyze the sliding energy[18]. Owing to their inherent characteristics, each kind of nanosheet stacking manifests a distinctive energy distribution along its optimized pathway, resulting in modified stable stacking modes (Fig. 1c and Supplementary Figs. 2–6). The most stable stacking mode identified for CuBDC-NO_2 nanosheets is $AB_{0.17}$ with a nanosheet sliding of 17% and a formation energy of −0.78 eV/atom (Fig. 1c), while for CuBDC-$(Br)_2$, AA is the most stable in stacking mode without sliding with the formation energy of −0.02 eV/atom (Supplementary Fig. 3). The simulated X-ray diffraction (XRD) patterns of various stacking modes exhibit regular variations, with gradually weakening the intensity of the (110)

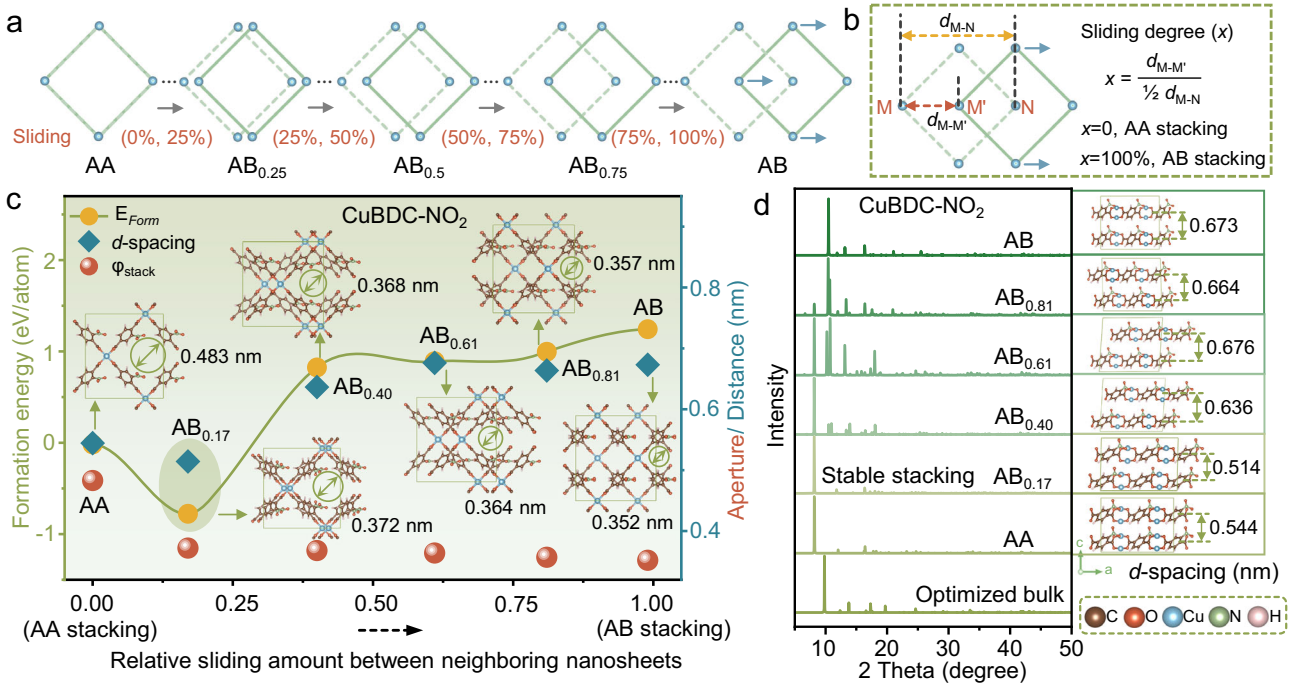

Fig. 1 | Simulated stacking process of MOF nanosheets. a Series of possible stacking modes, designated as AA and AB_x ($x \in (0, 1)$), with x indicating the sliding degree from 0 to 100% between neighboring MOF nanosheets. **b** Calculation of the sliding degree. $d_{M\text{-}M'}$ represents the distance between metal sites of M and M' along the sliding direction. $d_{M\text{-}N}$ represents the distance between metal sites of M to N in one nanosheet. **c** Sliding path of neighboring stacked CuBDC-NO_2 nanosheets with corresponding formation energy (E_{Form}), interlayer distance (*d*-spacing), stacking aperture (φ_{stack}) and stacking structure. **d** Simulated XRD patterns and stacking structures of the CuBDC-NO_2 nanosheets with different stacking modes.

https://doi.org/10.1038/s41467-024-54663-7

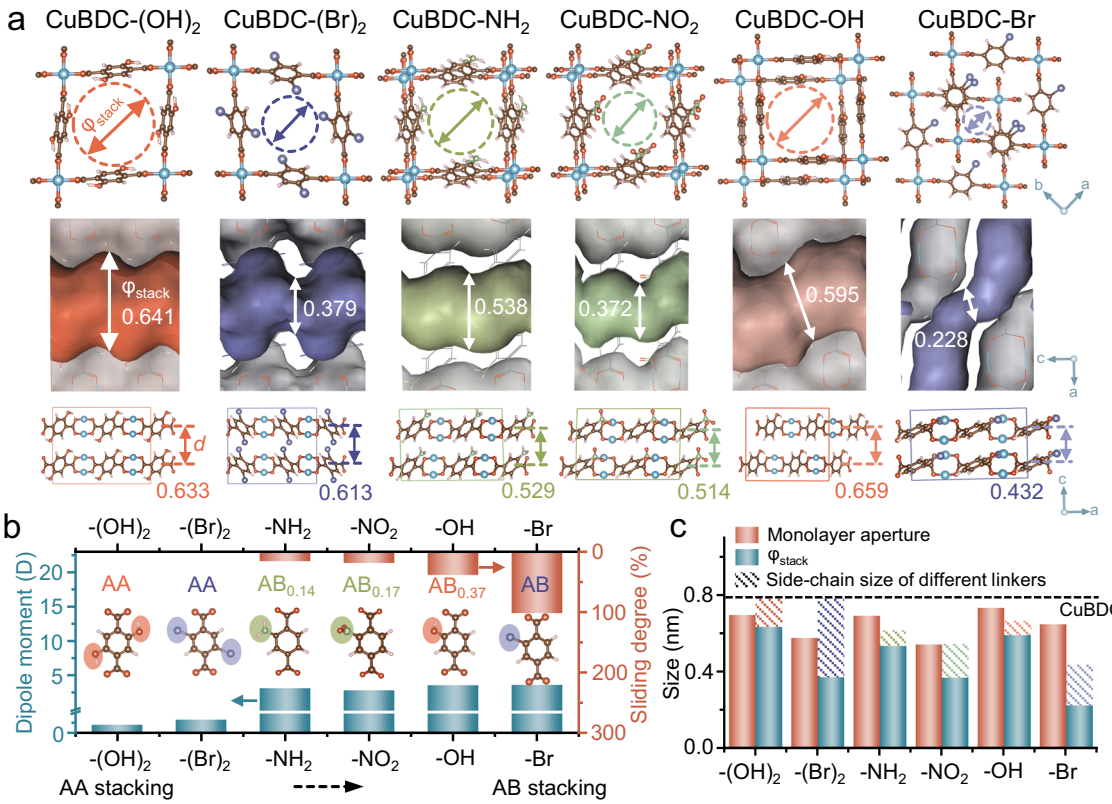

Fig. 2 | Regulation of MOF nanosheet stacks. a Stacking apertures (φ_{stack}) and *d*-spacing (*d*) of different MOF nanosheet stacks at the lowest formation energy. Values of φ_{stack} (nm) and *d* (nm) are given. **b** Effect of linker polarity on the sliding degree of various MOF nanosheet stacks. **c** Influence of the linker properties on monolayer-aperture and bilayer-stacking aperture. The dotted line represents the monolayer aperture of CuBDC. C, O, Cu, N, Br and H atoms depicted in Fig. 2a, b are colored in brown, red, blue, green, purple and pink, respectively.

characteristic peak and enhancing the intensity of the ($\bar{1}11$) characteristic peak correlated with increasing sliding (Fig. 1d and Supplementary Figs. 7–11). In the energy optimization process of nanosheet stacking, the smallest interlayer distance (*d*-spacing) can always be obtained in the most stable stacked structures for all six kinds of MOF nanosheets (Fig. 1c, d and Supplementary Figs. 2–11), although no obvious monotonic trends in the alteration of interlayer distances with sliding degree is evident, which is consistent with literature[19]. Concurrently, the stacking apertures tend to decrease as the sliding degree increases, the detailed discussion can be found in Fig. 2.

According to the simulation results of various MOF nanosheet stackings with lowest formation energy, the sliding degree of nanosheets follows the order of CuBDC-$(OH)_2$ = CuBDC-$(Br)_2$ < CuBDC-NH_2 < CuBDC-NO_2 < CuBDC-OH < CuBDC-Br, with a corresponding sliding of 0%, 0%, 14%, 17%, 37% and 100%, respectively (Fig. 2a, b and Supplementary Tables 2-7). As shown in Fig. 2b, the introduction of diverse side chains induces variations in linker polarity, with dipole moments in the order of BDC-$(OH)_2$ < BDC-$(Br)_2$ < BDC-NO_2 < BDC-NH_2 < BDC-OH < BDC-Br. With increasing linker polarity, the interaction between the neighboring nanosheets becomes stronger, resulting in enhanced interlayer steric hindrance[20,21], which promotes the neighboring MOF nanosheets to an AB stacking with increased staggering degree. For example, AB stacking observed in CuBDC-Br is attributed to the introduction of relatively high polar -Br groups, which causes greater interlayer steric hindrance, resulting in considerable steric repulsion[22]. Consequently, a greater degree of staggered stacking emerges to release this repulsive force. BDC-$(OH)_2$ and BDC-$(Br)_2$ display relatively weak polarity owing to the high symmetry of the functional groups, which results in small steric repulsion between the MOF nanosheets, favoring AA stacking without any sliding. Additionally, the size of the side chain of linkers also influences the sliding degree, where the bulkier side chain of BDC-NO_2 with relatively low polarity leads to a comparable sliding degree to that of BDC-NH_2.

Different stacking modes with different sliding degrees yield distinct stacking apertures (φ_{stack}), where CuBDC-$(OH)_2$, CuBDC-$(Br)_2$, CuBDC-NH_2, CuBDC-NO_2, CuBDC-OH and CuBDC-Br show stacking apertures of 0.641, 0.379, 0.538, 0.372, 0.595 and 0.228 nm, respectively (Fig. 2a, c). However, the alteration in an effective aperture of stacked nanosheets does not exhibit a monotonic decreasing trend with the increasing sliding degree, since it is also affected by the size of the side chain in the linker, resulting in reduced stacking apertures with a larger side chain under equivalent staggering degree of nanosheet stacks. As shown in Fig. 2c, the pore size of monolayer nanosheet is exclusively influenced by the side chain size, while the obtained stacking aperture of each kind of MOF nanosheet stacks is co-influenced by the side chain size and the staggering degree, presenting a decreasing trend in stacking aperture with an increased sliding degree after the combination of the two factors. For example, the CuBDC-$(OH)_2$ nanosheets with smaller-sized side chains and AA stacking give a large stacking aperture of 0.641 nm, while CuBDC-Br in AB stacking with a larger side chain yields the smallest stacking aperture of 0.228 nm.

Furthermore, distinct side chains affect interlayer interactions during nanosheet stacking, leading to varied interlayer distances. The CuBDC-$(OH)_2$, CuBDC-$(Br)_2$, CuBDC-NH_2, CuBDC-NO_2, CuBDC-OH and CuBDC-Br nanosheet stacks exhibit interlayer distance of 0.633, 0.613, 0.529, 0.514, 0.659 and 0.432 nm, respectively (Fig. 2a). The free spacing between neighboring nanosheets can be calculated after subtracting the monolayer thickness of each kind of MOF, giving values of < 0.2 nm which are too small for gas diffusion. Therefore, in this case,

gas molecules can only be transported through the one-dimensional (1D) vertical channels constructed by in-plane pores of stacked MOF nanosheets in the membrane (Supplementary Fig. 12).

Experimental preparation of MOF nanosheets and corresponding membranes

The above-simulated engineering of stacked MOF nanosheets with controlled in-plane pore size has been experimentally verified. CuBDC-$(OH)_2$, CuBDC-$(Br)_2$ and CuBDC-NO_2 are chosen from the above toolbox of six kinds of MOFs to assemble into membranes based on the efficacy of the stacked apertures in separating the target gas molecules. Two of whom (CuBDC-$(Br)_2$ and CuBDC-NO_2) present relatively small stacking aperture (0.379 nm and 0.372 nm) suitable for gas sieving, while the third one (CuBDC-$(OH)_2$) with relatively large stacking aperture of 0.641 nm is prepared for further comparison. In our study, those nanosheets are obtained in a direct bottom-up microwave-assisted synthesis (Supplementary Fig. 13), where the thickness of the nanosheets is more influenced by the Cu/linker ratio in solution (Supplementary Figs. 14–16). At higher metal/linker ratios, MOF crystals tend to grow in multiple layers. Conversely, at lower metal/linker ratios, the growth of MOF nanosheets along the vertical direction is inhibited, leading to the formation of ultrathin nanosheets[23]. Additionally, the reduced diffusion of metal ions and linkers at lower temperatures can also impede nanosheet growth in a vertical direction. Such nanosheet growth mechanism is consistent for three kinds of different materials. Fourier transform infrared (FTIR) spectroscopy confirms the chemical composition of the nanosheets (Fig. 3a), where the characteristic peaks associated with distinct functional groups on various linkers provide evidence for the successful coordination of linkers with metal ions[24,25]. These MOF nanosheets exhibit typical features of microporous materials and show excellent thermal stability (Supplementary Figs. 17, 18 and Supplementary Table 8). The lateral sizes of the CuBDC-$(OH)_2$, CuBDC-$(Br)_2$, and CuBDC-NO_2 nanosheets, measured via scanning electron microscopy (SEM) and transmission electron microscopy (TEM), are approximately 2, 0.6 and 3 μm, respectively (Fig. 3b–g), with thicknesses of 0.6, 0.7 and 0.7 nm (Supplementary Fig. 19), respectively. These microscopy findings are consistent with the theoretical monolayer thickness. The diffraction rings from the selected area electron diffraction (SAED) corresponding to $(\bar{2}01)$ plane can be distinctly observed in the as-synthesized three kinds of nanosheets (Fig. 3h–j). The measured *d*-spacing values of the CuBDC-$(OH)_2$, CuBDC-$(Br)_2$ and CuBDC-NO_2 nanosheets are 0.54, 0.46 and 0.54 nm, respectively, agreeing with the XRD results. Energy-dispersive X-ray spectroscopy (EDS) mapping results (Supplementary Figs. 20–22) also confirm the successful preparation of these nanosheets.

A series of corresponding membranes were assembled using the above prepared CuBDC-$(OH)_2$, CuBDC-$(Br)_2$ and CuBDC-NO_2 nanosheets on porous α-alumina (α-Al_2O_3) substrates using the hot-drop-coating approach, where the stability of the stacked nanosheets is mainly controlled by intermolecular forces. The SEM images of all membranes present a continuous layer morphology (Fig. 3k–m and Supplementary Fig. 23). The X-ray photoelectron spectroscopy (XPS) characterization of these nanosheet membranes could even detect Al signals from the underlying substrate (Fig. 3n), indicating that the membrane thicknesses are less than 10 nm. As shown in Fig. 3o, p, new peaks at 8.2° can be observed in the XRD patterns of the CuBDC-$(OH)_2$ and CuBDC-$(Br)_2$ nanosheet films, in addition to presenting $(\bar{2}01)$ reflection on the pore orientation, corresponding to the (110) reflection of the AA stacking mode, which cannot be found in the XRD patterns of the simulated AB stacking mode. The scattering signals well matched with AA stacking demonstrate that the CuBDC-$(OH)_2$ and CuBDC-$(Br)_2$ nanosheet films adopt AA stacking mode. For the CuBDC-NO_2 nanosheet film (Fig. 3q), the newly appeared diffraction peaks at 8.2° and 18.0°, corresponding to the (110) and $(\bar{1}30)$ reflections, respectively, match well with the XRD patterns of the simulated $AB_{0.17}$ stacking mode. Such experimental results are also in agreement with their corresponding simulated structures, where the nanosheets stack in the lowest formation energy. It has also demonstrated that it is reasonable and credible to predict the nanosheets stacking structure by DFT simulation, although it was carried out in a vacuum.

Experimental investigation on separation performance

In order to find out the optimal drop-coating temperature for membrane preparation, a detailed exploration was conducted on CuBDC-$(Br)_2$ as a typical representative. Figure 4a illustrates the separation performance of CuBDC-$(Br)_2$ nanosheet membranes prepared at different drop-coating temperatures for an equimolar H_2/CH_4 mixture. The optimal temperature for membrane preparation is found to be 70 °C, with a maximum H_2/CH_4 selectivity of 357 while maintaining the high H_2 permeance of 4.65×10^{-7} mol m^{-2} s^{-1} Pa^{-1} (Supplementary Table 9). A comparable trend is also observed for H_2/CO_2 separation (Supplementary Fig. 24). At relatively low temperatures, the slow evaporation rate of the solvent leads to the excessive aggregation of the nanosheets, resulting in the formation of defects, which decreases the separation performance, as evidenced by XRD associated with the $(\bar{2}01)$ orientation (Fig. 4a). At elevated temperatures, nanosheet deposition is heavily disturbed by the fast evaporation of the solvent, increasing the probability of defect formation in the membrane and thus diminishing gas selectivity. Therefore, 70 °C is chosen as the optimal temperature for drop-coating to prepare also the other two kinds of nanosheet membranes in this study.

The H_2 separation performance of as-synthesized CuBDC-$(OH)_2$ and CuBDC-NO_2 nanosheet membranes has been compared with that of CuBDC-$(Br)_2$. With increasing linker polarity (BDC-$(OH)_2$ < BDC-$(Br)_2$ < BDC-NO_2), the H_2 permeance decreases while gas selectivity for H_2/CO_2 and H_2/CH_4 mixtures increases accordingly (Fig. 4b). The CuBDC-$(OH)_2$ nanosheet membrane exhibits the highest H_2 permeance of 5.63×10^{-7} mol m^{-2} s^{-1} Pa^{-1}, whereas the CuBDC-NO_2 nanosheet membrane shows the highest selectivity for both H_2/CO_2 (266) and H_2/CH_4 (536) among the three kinds of MOF nanosheet membranes under study (Supplementary Tables 10 and 11). This finding can be attributed to the different polarity of linkers, influencing the neighboring nanosheet sliding degree, thus consequently altering the effective stacking aperture of membranes, which causes different separation performances. The BDC-NO_2 linker displays the highest polarity with a stronger repulsion, resulting in an $AB_{0.17}$ stacking mode of the nanosheet stacks with sliding of 17%, which yields a suitable pore size of 0.372 nm for H_2 sieving. On the contrary, the CuBDC-$(OH)_2$ and CuBDC-$(Br)_2$ nanosheet membranes give an AA stacking without sliding due to the small polarity of linkers, leading to stacking apertures of 0.641 and 0.379 nm (also affected by the size of side chains), respectively. It can be noted that the CuBDC-NO_2 and CuBDC-$(Br)_2$ nanosheet membranes manifest higher H_2/CH_4 selectivity than the CuBDC-$(OH)_2$ nanosheet membrane (Fig. 4b) due to the appropriate stacking apertures, which are smaller than the kinetic diameter of CH_4 (0.38 nm). These experimental results agree with the above findings from simulations and support the influence of linker polarity on the nanosheet stacking modes (Figs. 1 and 2).

Moreover, the interaction between gas and MOF nanosheets also influences the gas separation performance of the membranes. The influence of linker polarity and the stacking mode of 2D MOFs on the gas adsorption heat and membrane separation performance for H_2/CO_2 and H_2/CH_4 mixtures have been systematically explored using the Widom test particle insertion method[26]. As shown in Fig. 4c, the adsorption heat (Q_{st}, kJ/mol) of CO_2 molecules is obviously influenced by the polarity of the linkers, compared with that of H_2 and CH_4. For most stacking modes, with the increased polarity of the linkers (BDC-$(OH)_2$ < BDC-$(Br)_2$ < BDC-NO_2 < BDC-NH_2 < BDC-OH < BDC-Br, Fig. 2b), the adsorption heat of CO_2 with MOF nanosheets increases due to enhanced interaction. For the MOF nanosheet with relatively high

https://doi.org/10.1038/s41467-024-54663-7

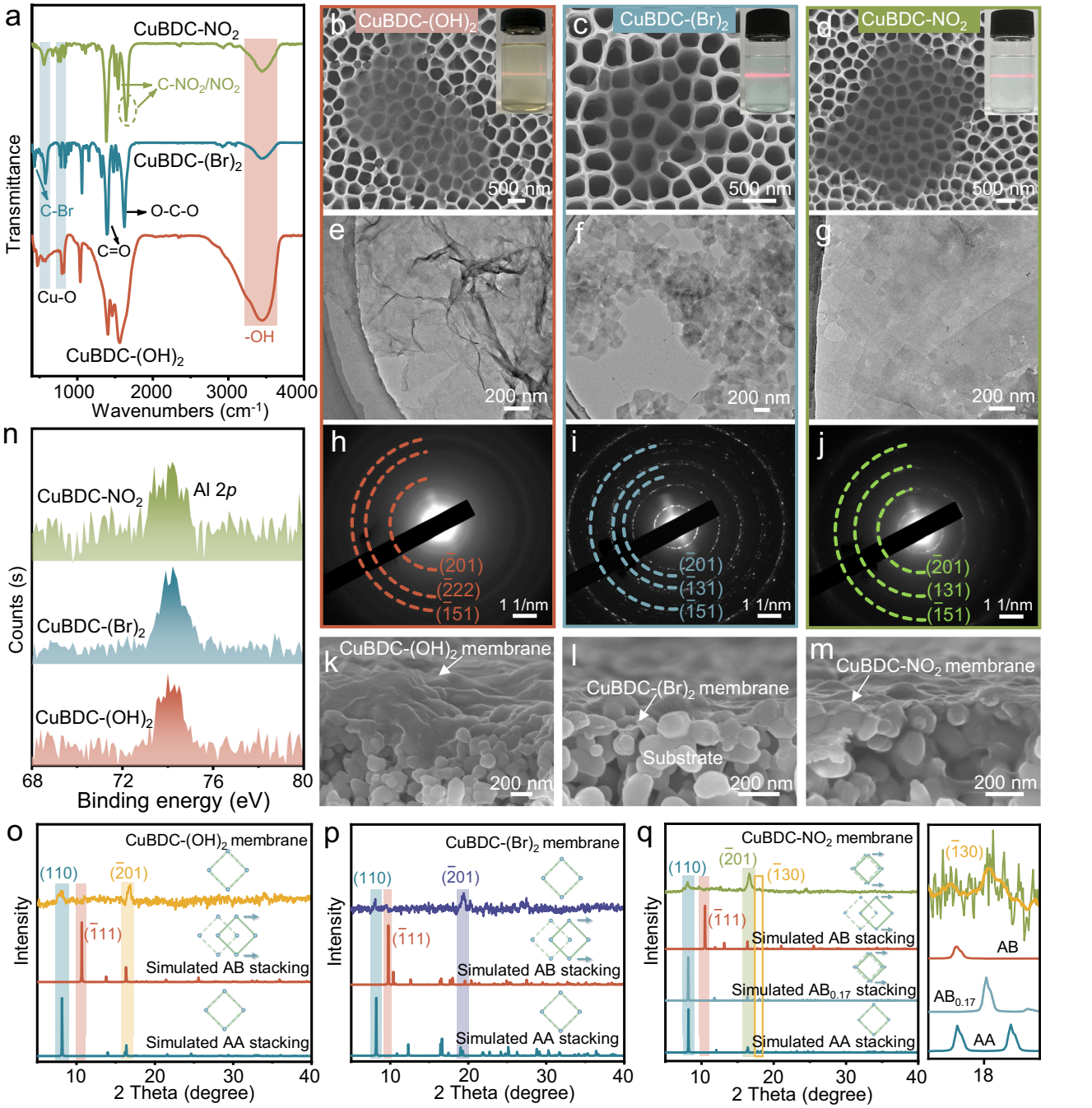

Fig. 3 | Characterizations of MOF nanosheets and corresponding membranes. **a** FTIR spectra of the CuBDC-$(OH)_2$, CuBDC-$(Br)_2$ and CuBDC-NO_2 nanosheets. SEM images (**b**–**d**), TEM images (**e**–**g**) and SAED patterns (**h**–**j**) of the as-synthesized CuBDC-$(OH)_2$, CuBDC-$(Br)_2$ and CuBDC-NO_2 nanosheets, respectively. SEM cross-sectional view (**k**–**m**), high-resolution Al 2*p* XPS spectra (**n**) and XRD patterns (**o**–**q**) of the CuBDC-$(OH)_2$, CuBDC-$(Br)_2$ and CuBDC-NO_2 nanosheets stacks. The enlarged area on the right of Fig. 3q corresponds to the yellow rectangular wireframe area depicted on the left.

polarity of the linker, such as CuBDC-Br, the adsorption heat of CO_2 molecules with nanosheets increases sharply when the stacking modes change from AA to AB stacking. It can be attributed that an increasing number of adsorption sites are exposed with increased staggering degree, leading to enhanced interaction between gas molecules and nanosheets. For the other five kinds of MOF nanosheets, there is no significant difference in the adsorption heat of gases (including CO_2, H_2 and CH_4) in various stacking modes, only with a fluctuation ratio of approximately 20% (Supplementary Fig. 25).

For H_2/CH_4 separation through the CuBDC-$(Br)_2$ and CuBDC-NO_2 nanosheets membrane with an effective aperture of 0.379 nm and 0.372 nm, which are smaller than the kinetic diameter of CH_4 (0.38 nm), size sieving is the main separation mechanism. For H_2/CO_2 separation, where the kinetic diameter of CO_2 (0.33 nm) is smaller than all the effective apertures of three kinds of MOF nanosheet membranes, the mechanism of gas separation is predominated by gas adsorption. As is known, higher adsorption heat of CO_2 indicates stronger interaction with the MOF nanosheets, leading to increased gas diffusion resistance, thus resulting in markedly lower CO_2 permeance and higher H_2/CO_2 selectivity. Taking CuBDC-NO_2 nanosheets membrane, for example, it presents relatively high CO_2 adsorption observed in both adsorption isotherms (Supplementary Fig. 26) and Monte Carlo (MC) simulation

https://doi.org/10.1038/s41467-024-54663-7

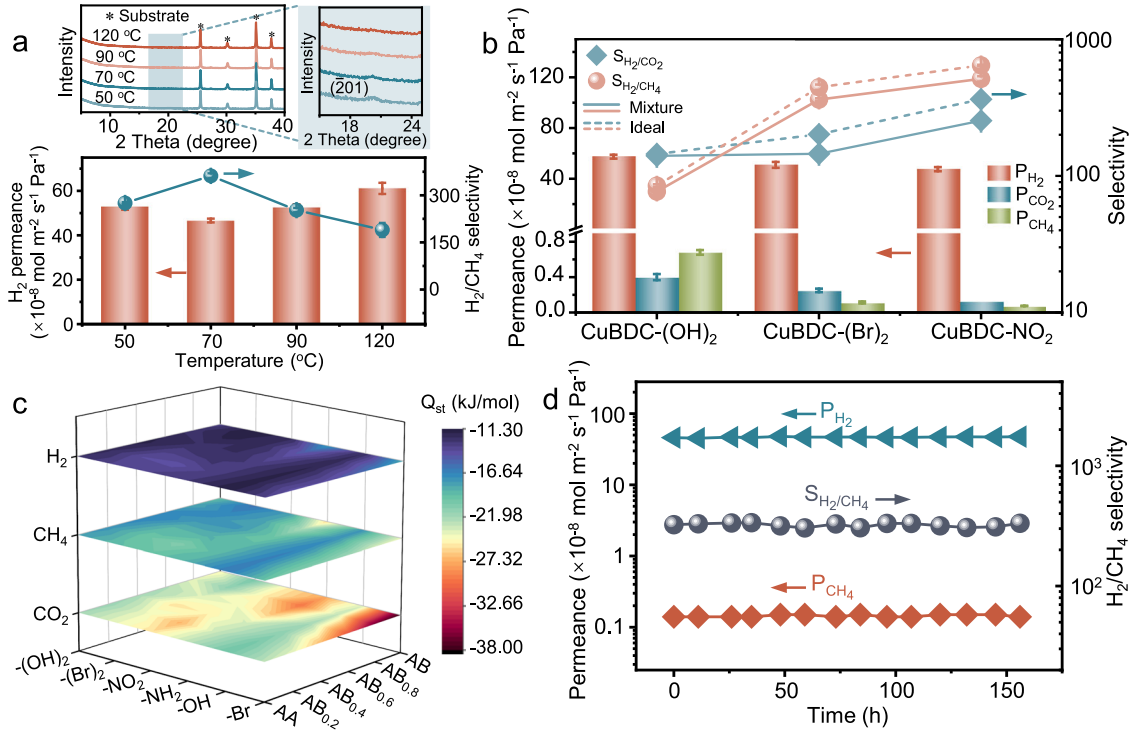

Fig. 4 | Gas separation performance of MOF nanosheet membranes. a XRD patterns and gas separation performance of the CuBDC-$(Br)_2$ nanosheet membranes prepared at different drop-coating temperatures for H_2/CH_4 binary mixture. **b** Comparison of gas separation performance of the CuBDC-$(OH)_2$, CuBDC-$(Br)_2$ and CuBDC-NO_2 nanosheet membranes. The error bars of Fig. 4a, b represent the standard deviation derived from measurements of three membranes prepared under identical conditions. **c** 3D adsorption heat (Q_{st}, kJ/mol) map of H_2, CH_4 and CO_2 with CuBDC-$(OH)_2$, CuBDC-$(Br)_2$, CuBDC-NO_2, CuBDC-NH_2, CuBDC-OH and CuBDC-Br nanosheets in different stacking modes. **d** Stability of the CuBDC-$(Br)_2$ nanosheet membrane in H_2/CH_4 separation.

(Supplementary Fig. 27) results. Consequently, it exhibits a relatively high H_2/CO_2 selectivity of 266, attributed to the relatively strong interaction of CO_2 molecules with MOF nanosheets.

The separation performance of the CuBDC-$(Br)_2$ nanosheet membrane is further systematically investigated at various H_2 concentrations in the feed mixture and various temperatures (Supplementary Figs. 28 and 29). Both selectivity of H_2/CH_4 and H_2/CO_2 separation, as well as the H_2 permeance exhibit an increasing trend with the rise of H_2 concentration in the feed (Supplementary Fig. 28). The increase in temperature leads to elevated gas permeance and decreased selectivity (Supplementary Fig. 29a), attributed to the enhanced diffusion of H_2 and CO_2 through the membrane at elevated temperatures. The apparent activation energy (E_{act}) of H_2 and CO_2 permeation through the CuBDC-$(Br)_2$ nanosheet membrane is calculated according to the Arrhenius equation, revealing that H_2 molecules can permeate through the membrane much easier than CO_2 molecules (Supplementary Fig. 29b). The separation performance of the CuBDC-$(Br)_2$ nanosheet membrane can be almost recovered when the operation temperature is back, indicating the good thermal stability of the CuBDC-$(Br)_2$ nanosheet membrane. Moreover, the gas permeance and selectivity of the CuBDC-$(Br)_2$ nanosheet membrane show negligible fluctuations during testing up to 150 h (Fig. 4d and Supplementary Fig. 30), confirming its excellent long-term stability. It should be noted that there is no pore blockage, although the interaction between gas molecules and framework exists.

The influence of feed pressure on the H_2/CO_2 separation has also been investigated, showing that both H_2 and CO_2 permeance increase significantly with rising feed pressure, while H_2/CO_2 selectivity declines sharply (Supplementary Fig. 31). It is attributed to the presence of non-selective transport pathways in the CuBDC-$(Br)_2$ nanosheet membrane, allows Knudsen and viscous flow dominating the membrane separation performance when the transmembrane pressure difference is greater than zero[27–30]. To the best of our knowledge, there is only a few studies having explored this issue[28,31–33], where most membrane separation performance deteriorated under increased feed pressure. For the practical applications of H_2/CO_2 separation where the operation pressure is larger than 10 bar, the membrane with good anti-pressure stability is urgently needed. The development of defect-free (or at least less defective) nanosheet membranes should be alternative, where novel membrane assembly strategy is required. Moreover, the type of monolayer nanosheet membranes without stacking defects also holds promise for addressing the pressure resistance challenges in the future[34–36].

In summary, we have demonstrated that the stacking modes of MOF nanosheets with in-plane pores can be accurately controlled utilizing differences in linker polarity. Both theoretical calculations and experimental findings show that with increasing linker polarity, the interaction between the nanosheets is enhanced, which facilitates the neighboring nanosheets to stack in AB mode, thereby achieving an effective regulation of the stacking aperture. Among a series of CuBDC-based nanosheets with different linkers, the CuBDC-NO_2 nanosheet exhibits $AB_{0.17}$ stacking with a reduced stacking aperture of 0.372 nm, which is suitable for efficient H_2 sieving. The assembled CuBDC-NO_2 nanosheet membrane exhibits promising H_2/CO_2 and H_2/CH_4 selectivity of 266 and 536, respectively, maintaining a high H_2 permeance of 4.44×10^{-7} mol m^{-2} s^{-1} Pa^{-1}. This work represents the precise and controlled engineering of the stacking modes of MOF nanosheets, with the universality of diverse 2D materials. More importantly, tuning the stacking mode endows the MOF nanosheet stacks with new functions and properties, expanding their potential applications in broader fields.

Methods

Preparation of the CuBDC-$(OH)_2$ nanosheets

Copper(II) nitrate hydrate ($Cu(NO_3)_2 \cdot 3H_2O$) (0.07 g) was dissolved in the mixture of acetonitrile (21.0 mL) and N,N-dimethylformamide (DMF) (7.0 mL). 2,5-dihydroxyterephthalic acid (BDC-$(OH)_2$) (0.21 g)

was dissolved in the mixture of acetonitrile (7.0 mL) and DMF (21.0 mL). These two solutions were completely mixed by ultrasound and transferred into a special Teflon vessel for microwave reactions. CuBDC-$(OH)_2$ nanosheets were synthesized at 50 °C for 30 min by microwave hydrothermal reaction. The other variable conditions include temperatures (60, 80, 90 and 100 °C), and metal/linkers ratios (1:1, 1:1.5, 1:3, 1:7, 1:30 and 1:35). After thermal treatment, the vessel was naturally cooled to room temperature. All nanosheet products obtained were isolated by centrifugation at 11180 × g for 30 min. The CuBDC-$(OH)_2$ nanosheets were washed with DMF for several times and then dichloromethane (CH_2Cl_2) for several times, to effectively remove residual linkers and solvents (Supplementary Fig. 32a). The washed nanosheets were dispersed in CH_2Cl_2 solution and stored.

Preparation of the CuBDC-$(Br)_2$ nanosheets

$Cu(NO_3)_2{\cdot}3H_2O$ (0.005 g) was dissolved in the mixture of acetonitrile (21.0 mL) and DMF (7.0 mL). 2,5-dibromoterephthalic acid (BDC-$(Br)_2$) (0.21 g) was dissolved in the mixture of acetonitrile (7.0 mL) and DMF (21.0 mL). These two solution were completely mixed by ultrasound and transferred into a special Teflon vessel for microwave reactions. CuBDC-$(Br)_2$ nanosheets were synthesized at 80 °C for 30 min by microwave hydrothermal reaction. The other variable conditions include temperatures (50 and 65 °C), and metal/linkers ratios (1:1, 1:1.75, 1:7, 1:21, 1:30, 1:35 and 1:42). After thermal treatment, the vessel was naturally cooled to room temperature. All nanosheet products obtained were isolated by centrifugation at 111,80 × g for 30 min. The CuBDC-$(Br)_2$ nanosheets were washed with DMF for several times and then CH_2Cl_2 for several times, to effectively remove residual linkers and solvents (Supplementary Fig. 32b). The washed nanosheets were dispersed in CH_2Cl_2 solution and stored.

Preparation of the CuBDC-NO_2 nanosheets

$Cu(NO_3)_2{\cdot}3H_2O$ (0.01 g) was dissolved in acetonitrile (21.0 mL) and DMF (7.0 mL). Nitroterephthalic acid (BDC-NO_2) (0.21 g) was dissolved in acetonitrile (7.0 mL) and DMF (21.0 mL). These two solution were completely mixed by ultrasound and transferred into a special Teflon vessel for microwave reactions. CuBDC-NO_2 nanosheets were synthesized at 75 °C for 30 min by microwave hydrothermal reaction. The other variable conditions include temperatures (80 and 100 °C), and metal/linkers ratios (1:1, 1:7, 1:21, 1:35 and 1:42). After thermal treatment, the vessel was naturally cooled to room temperature. All nanosheet products obtained were isolated by centrifugation at 11,180 × g for 30 min. The CuBDC-NO_2 nanosheets were washed with DMF for several times and then CH_2Cl_2 for several times, to effectively remove residual linkers and solvents (Supplementary Fig. 32c). The washed nanosheets were dispersed in CH_2Cl_2 solution and stored.

Membranes preparation

The MOF nanosheets membranes were prepared via the hot drop coating technique. Those nanosheet solution (with the same concentration) were individually deposited onto the surface of α-Al_2O_3 support heated to a certain temperature, and the support was kept heating at a constant temperature on a heating plate. Different heating support temperatures from 50 °C to 120 °C were investigated. The prepared nanosheet membranes were dried at the corresponding drop coating temperature.

Characterizations

The structures of those nanosheets were investigated by XRD (Rigaku SmartLab) with Cu Kα radiation (λ = 0.154056 nm) at 40 kV and 40 mA. FTIR (Thermo Scientific IS50) was used to study the chemical composition of the nanosheets. The morphology of the nanosheets and membranes were observed using a field emission SEM (FESEM, Hitachi SU8220) at an accelerating voltage of 10 kV and a current of 10 μA. TEM (Bruker Nano GmbH Berlin, Germany) and SAED images were also captured. The elemental distributions were characterized through EDS mapping. The nanosheet thickness was observed by atomic force microscopy (AFM Bruker Multimode 8). Thermogravimetric analyses instrument (TGA, NETZSCH TG 209F1 Libra) was used to analyze the thermal stability of the nanosheets in the temperature range of 30–900 °C with a heating rate of 10 K min^{-1} under flowing N_2 atmosphere. A physisorption analyzer (ASAP 2460 Version 3.01) was used to collect the N_2 adsorption-desorption isotherms at 77 K. Before measurement, the samples were degassed at 120 °C under vacuum for 6 h.

Separation performance

Gas separation performance of the membranes were evaluated using a gas chromatograph (Agilent 7890 A) through the Wicke-Kallenbach method[37]. The nanosheets membranes were sealed in a module sealed with O-rings. For a single-gas permeation measurement, a volumetric flow rate of 25 mL min^{-1} gas was applied to the feed side of the membrane, and the permeate gas was removed from the permeate side by the sweep gas. Pressures at both the feed side and permeate side were maintained at 1 bar. The gas permeance, P_i (mol m^{-2} s^{-1} Pa^{-1}), is defined as (1):

$$P_i = \frac{N_i}{\Delta P_i \cdot A} \tag{1}$$

where N_i (mol s^{-1}) is the molar flow rate of component i, ΔP_i (Pa) is the transmembrane pressure difference of component i, and A (m^2) is the effective membrane area for testing. The ideal selectivity ($S_{i/j}$) is calculated from the relation between the permeance of component i and component j.

$$S_{i/j} = \frac{P_i}{P_j} \tag{2}$$

For mixture separation, the equimolar H_2/CO_2 or H_2/CH_4 binary mixture was feed into the shell side of the membrane, where the prepared nanosheet membranes were fixed in a module sealed with O-rings. A gas mixture with flow rate ratio of 1:1 was applied to the feed side of the membrane, and the permeate gas was removed from the permeate side by the sweep gas. The feed flow rate was kept constant with a total volumetric flow rate of 50 mL min^{-1} (each gas, 25 mL min^{-1}). Pressures at both the feed side and permeate side were maintained at 1 bar. The driving force for gas permeation is the partial pressure difference of each component across the membrane, which results from the different gas concentrations between the feed side and the permeate side. Herein, the partial pressure difference of each gas is 0.5 bar, although there is no total pressure difference across the membrane. A gas chromatograph was used to measure the concentration of each gas on the permeate side. The selectivity, $\alpha_{i,j}$ of the gas pairs is defined as the molar ratio of the components (i, j) in the permeate side, divided by the molar ratio of the components (i, j) in the feed side:

$$\alpha_{i,j} = \frac{X_{i,\,perm}/X_{j,\,perm}}{X_{i,\,feed}/X_{j,\,feed}} \tag{3}$$

Data availability

Further data that support the findings of this study are available on request from the corresponding author. Source Data are provided with this paper.

References

1. Yang, L. et al. Energy-efficient separation alternatives: metal-organic frameworks and membranes for hydrocarbon separation. *Chem. Soc. Rev.* **49**, 5359–5406 (2020).

2. Sholl, D. S. & Lively, R. P. Seven chemical separations to change the world. *Nature* **532**, 435–438 (2016).
3. Koros, W. & Zhang, C. Materials for next-generation molecularly selective synthetic membranes. *Nat. Mater.* **16**, 289–297 (2017).
4. Werber, J., Osuji, C. & Elimelech, M. Materials for next-generation desalination and water purification membranes. *Nat. Rev. Mater.* **1**, 16018 (2016).
5. Liu, G. et al. Eliminating lattice defects in metal-organic framework molecular-sieving membranes. *Nat. Mater.* **22**, 769–776 (2023).
6. Gin, D. L. & Noble, R. D. Designing the next generation of chemical separation membranes. *Science* **332**, 674–676 (2011).
7. Lee, T. H. & Smith, Z. P. Better standards are needed for membrane materials. *Nat. Mater.* **23**, 11–12 (2024).
8. Yang, Z. et al. ZIF-62 glass foam self-supported membranes to address CH_4/N_2 separations. *Nat. Mater.* **22**, 888–894 (2023).
9. Park, H. B. et al. Maximizing the right stuff: The trade-off between membrane permeability and selectivity. *Science* **356**, eaab0530 (2017).
10. Peng, Y. et al. Metal-organic framework nanosheets as building blocks for molecular sieving membranes. *Science* **346**, 1356–1359 (2014).
11. Varoon Agrawal, K. et al. Dispersible exfoliated zeolite nanosheets and their application as a selective membrane. *Science* **334**, 72–75 (2011).
12. Jeon, M. Y. et al. Ultra-selective high-flux membranes from directly synthesized zeolite nanosheets. *Nature* **543**, 690–694 (2017).
13. Ying, Y. et al. Ultrathin two-dimensional membranes assembled by ionic covalent organic nanosheets with reduced apertures for gas separation. *J. Am. Chem. Soc.* **142**, 4472–4480 (2020).
14. Peng, Y. et al. Two-dimensional metal-organic framework nanosheets for membrane-based gas separation. *Angew. Chem. Int. Ed.* **56**, 9757–9761 (2017).
15. Wang, X. et al. Reversed thermo-switchable molecular sieving membranes composed of two-dimensional metal-organic nanosheets for gas separation. *Nat. Commun.* **8**, 14460 (2017).
16. Song, S. et al. Tuning the stacking modes of ultrathin two-dimensional metal-organic framework nanosheet membranes for highly efficient hydrogen separation. *Angew. Chem. Int. Ed.* **62**, e202312995 (2023).
17. Rodenas, T. et al. Metal-organic framework nanosheets in polymer composite materials for gas separation. *Nat. Mater.* **14**, 48–55 (2015).
18. Henkelman, G. et al. A climbing image nudged elastic band method for finding saddle points and minimum energy paths. *J. Chem. Phys.* **113**, 9901–9904 (2000).
19. Tao, P. et al. Stacking stability of MoS_2 bilayer: An ab initio study. *Chin. Phys. B* **23**, 106801 (2014).
20. Fu, H. et al. Mechanism for selective binding of aromatic compounds on oxygen-rich graphene nanosheets based on molecule size/polarity matching. *Sci. Adv.* **8**, eabn4650 (2022).
21. Wu, X. et al. Control interlayer stacking and chemical stability of two-dimensional covalent organic frameworks via steric tuning. *J. Am. Chem. Soc.* **140**, 16124–16133 (2018).
22. Fan, W. et al. Multivariate polycrystalline metal-organic framework membranes for CO_2/CH_4 separation. *J. Am. Chem. Soc.* **143**, 17716–17723 (2021).
23. Zhang, Y. et al. Influence of the 2-methylimidazole/zinc nitrate hexahydrate molar ratio on the synthesis of zeolitic imidazolate framework-8 crystals at room temperature. *Sci. Rep.* **8**, 9597 (2018).
24. Zhou, X. et al. Molecular scalpel to chemically cleave metal-organic frameworks for induced phase transition. *J. Am. Chem. Soc.* **143**, 6681–6690 (2021).
25. Wu, W. et al. Vapor-phase linker exchange of metal-organic frameworks. *Sci. Adv.* **6**, eaax7270 (2020).
26. Widom, B. Some topics in the theory of fluids. *J. Chem. Phys.* **39**, 2808–2812 (1963).
27. Wang, B. et al. A super-permeable and highly-oriented SAPO-34 thin membrane prepared by a green gel-less method using high-aspect-ratio nanosheets for efficient CO_2 capture. *Chem. Eng. J.* **442**, 136336 (2022).
28. Zhou, Y. et al. Fast hydrogen purification through graphitic carbon nitride nanosheet membranes. *Nat. Commun.* **13**, 5852 (2022).
29. Wang, B. et al. Improved AlPO-18 membranes for light gas separation. *J. Mater. Chem. A* **3**, 12205–12212 (2015).
30. Poshusta, J. C. et al. Separation of light gas mixtures using SAPO-34 membranes. *AIChE J.* **46**, 779–789 (2000).
31. Ding, L. et al. MXene molecular sieving membranes for highly efficient gas separation. *Nat. Commun.* **9**, 155 (2018).
32. Shen, J. et al. 2D MXene nanofilms with tunable gas transport channels. *Adv. Funct. Mater.* **28**, 1801511 (2018).
33. Qu, K. et al. Self-crosslinked MXene hollow fiber membranes for H_2/CO_2 separation. *J. Membr. Sci.* **638**, 119669 (2021).
34. Liu, Q. et al. Unit-cell-thick zeolitic imidazolate framework films for membrane application. *Nat. Mater.* **22**, 1387–1393 (2023).
35. Huang, S. et al. Single-layer graphene membranes by crack-free transfer for gas mixture separation. *Nat. Commun.* **9**, 2632 (2018).
36. Lee, W.-C. et al. Centimeter-scale gas-sieving nanoporous single-layer graphene membrane. *J. Membr. Sci.* **618**, 118745 (2021).
37. Zhou, S. et al. Asymmetric pore windows in MOF membranes for natural gas valorization. *Nature* **606**, 706–712 (2022).

Acknowledgements

Y.W. acknowledges the funding from the National Key Research and Development Program (2021YFB3802500), the Natural Science Foundation of China (U23A20115, 22078107 and 22022805), the Natural Science Foundation of Guangdong Province (2024A1515012724) and the Guangzhou Municipal Science and Technology Project (2024A04J6251). L.L. acknowledges the funding from the Natural Science Foundation of China (22078104) and Natural Science Foundation of Guangdong Province (2024A1515012725).

Author contributions

W.W. conceived the research idea and wrote the manuscript. W.W., X.Y., and L.D. conducted the experiments and characterizations. X.C. performed the simulations. W.W., X.C., Y.W., and L.L. analyzed the data. L.L., Y.W., and H.W. directed this work, and contributed to the review and editing of the manuscript. All authors contributed to the manuscript.

Competing interests

The authors declare no competing interests.

Additional information

Supplementary information The online version contains supplementary material available at https://doi.org/10.1038/s41467-024-54663-7.

Correspondence and requests for materials should be addressed to Yanying Wei, Libo Li or Haihui Wang.

Peer review information *Nature Communications* thanks Ilknur Eruçar and the other, anonymous, reviewer(s) for their contribution to the peer review of this work. A peer review file is available.